J Mater Sci: Mater Electron **(2025) 36:1869**

Synthesis, DFT calculations, magnetic, and high-frequency dielectric properties of nickel ferrite ($NiFe_2O_4$)

Muhammad Asif[1], Wasif Irshad[1], Muhammad Iqbal Asif[1], Atiq ur Rehman[2], Rasmiah S. Almufarij[3], Yousef Mohammed Alanazi[4], Rizwan Ul Hassan[5,*], Mukhtar Ahmad[1], Ghulam Abbas Ashraf[6], Doniyor Jumanazarov[7], and Farruh Atamurotov[8,9,10]

[1] *Department of Physics, COMSATS University Islamabad Lahore Campus, Lahore 54000, Pakistan*
[2] *Department of Physics, Emerson University Multan, Multan, Pakistan*
[3] *Department of Chemistry, College of Science, Princess Nourah Bint Abdulrahman University, P.O. Box 84428, Riyadh 11671, Saudi Arabia*
[4] *Chemical Engineering Department, College of Engineering, King Saud University, Riyadh, Saudi Arabia*
[5] *Department of Chemical and Biological Engineering, Gachon University, Seongnam, Gyeonggi-do 13120, Republic of Korea*
[6] *Low Dimensional Materials Research Center at, Khazar University, AZ1096 Baku, Azerbaijan*
[7] *Urgench State University, Kh. Alimdjan Str. 14, 220100 Urgench, Uzbekistan*
[8] *University of Tashkent for Applied Sciences, Str. Gavhar 1, 100149 Tashkent, Uzbekistan*
[9] *Kimyo International University in Tashkent, Shota Rustaveli Str. 156, Tashkent 100121, Uzbekistan*
[10] *Tashkent State Technical University, Tashkent, 100095, Uzbekistan*

Received: 28 February 2025
Accepted: 28 August 2025

© The Author(s), under exclusive licence to Springer Science+Business Media, LLC, part of Springer Nature, 2025

ABSTRACT

Nickel ferrite ($NiFe_2O_4$), one of the very important ferrite materials, has been considered for many applications, such as high-density magnetic storage media, MRI contrast agents, color imaging, ferrofluids, high-frequency devices, magnetic refrigerators, catalysts, and microwave devices. We applied theoretical and experimental approaches to study the structural, magnetic, dielectric, and electrical properties of nickel ferrite ($NiFe_2O_4$). The sol–gel method was employed to synthesize nickel ferrite ($NiFe_2O_4$). Various experimental analyses, including X-ray diffraction (XRD), Fourier transform infrared (FT-IR) spectroscopy, scanning electron microscopy (SEM), and vibrating magnetometry (VSM), were carried out to investigate its different properties. Theoretical approaches such as Density Functional Theory (DFT) using CASTEP codes with other approximations, including generalized gradient approximation (GGA), local spin-density approximation (LSDA), and local density approximation (LDA), were employed. XRD showed the FCC structure of the prepared material with a lattice constant of 8.20 Å that corresponds to the fd-3 m space group. The FT-IR spectrum confirmed the absorption peak at 598 cm^{-1} because of octahedral sites present in the inverse spinel $NiFe_2O_4$. For the investigation of surface morphology, SEM was used that

---

Address correspondence to E-mail: rizwanhassan72@gmail.com; drmuhammadasif@cuilahore.edu.pk

https://doi.org/10.1007/s10854-025-15755-2

Published online: 15 October 2025

showed the agglomeration with varying sizes of particles. VSM confirmed the soft magnetic nature of the prepared material with its magnetic moment of 2.63, and the M–H loop was used to derive the magnetic properties of the sample. Using various approximations, all work was done in CASTEP code and theoretically DFT was employed. We had shifted to using GGA, which yields dependable consequences that are in best accord with the experimental results, because LSDA failed to explain the magnetic structure of the current compound. These outcomes include band gap, lattice parameters, electrical properties, and magnetic properties. Dielectric constant and dielectric loss were observed to decrease with frequency and increase with temperature, following Koop's theory. Furthermore, AC conductivity was also studied at varying frequencies at different temperatures.

1 Introduction

Nanomaterial is the focus of intense research due to its unique chemical and physical properties, synthesis, and applications. These materials have more attractions because of their scientific and technological importance. Nanocrystalline spinel ferrites with the common formula MFe_2O_4 (M = Ni, Zn, Mn, Co, Mg, etc.) are the most significant magnetic materials [1–5]. The spinel structure has a space group Fd3m. The cubic unit cell is made up of 56 atoms, 32 oxygen anions distributed in a cubic close-packed structure, and 24 cations that take up 16 of the 32 octahedral sites (B-sites) and 8 of the 64 tetrahedral sites (A-sites) [6–11]. Nickel ferrite (NFe_2O_4) is an important ferrite material that has been considered for numerous applications, including MRI contrast agents, high-density magnetic storage media, color imaging magnetic refrigerators, ferrofluids, catalysts, high-frequency devices, and microwave devices [12]. The nickel ferrite ($NiFe_2O_4$) was prepared using various chemical routes. A specific study has been made to synthesis $NiFe_2O_4$ nanoparticles. The magnetic properties of the synthesized material mainly depend upon particle size and synthesis routes. Ferromagnetic behavior is a common feature, with values close to saturation magnetization when compared to the relevant bulk material. The microstructure and composition affect the properties of the prepared material that is sensitive to the preparation methodology used in its preparation. There are many synthesis methods available to prepare the required material, including the sol–gel auto-combustion method, citric acid combustion method, organic gel-thermal decomposition method, hydrothermal method, co-precipitation method, gel-assisted hydrothermal route, thermolysis, wet-chemical co-precipitation technique, self-propagating, and microemulsion [13]. In this research article, the nickel ferrites were prepared using the sol–gel auto-combustion method, which is a sole combination of chemical gelation and ignition process. The main advantages of this method are cost-effectiveness, simple preparation, and gentle chemistry routes resulting in homogeneous and fine powder. Its ability to produce single-phase nanoparticles of nickel ferrites with controllable particle size and size distribution advances its capability in a wide range of technological applications [14]. Ferrites have the benefit of being less expensive and performing better than other items. They can be used as a black pigment and contrast agent in MRI scans [15]. The general formula for spinel ferrite with a crystalline FCC structure is $A^{2+}B_2^{3+}O_4$, where A and B are metal cations. The magnetic characteristics of nanoferrites include A–A, B–B, and A–B contacts, among other exchange interactions among sub-lattices. Researchers are working on several spinel ferrites uses. Zinc ferrite nanoparticles (ZNF) coated with oleic acid have a cubic shape. M–H loops serve as an example of the processed material's paramagnetic properties. At a minimum dosage rate of 8 mg/ml, the produced substance can be used to treat cancer and hyperthermia [16]. Since nanosized nickel ferrites have better chemical and physical characteristics than other ferrites, they are widely employed as materials for electronic applications. The specific heating, melting temperature, and expansion coefficients of nickel ferrite are comparatively high based on basic physicochemical properties.

However, they have low saturation magnetization, low Curie temperature, small coercivity, large electrical resistivity, small eddy current losses, and large electrochemical strength [17–19]. Because of the peculiar technological and fundamental properties, nickel ferrite ($NiFe_2O_4$) is of immense interest to researchers. It is understood that $NiFe_2O_4$ (NFO) possesses inverse spinel structures where Ni^{2+} cations are found within the B-sites and Fe^{3+} ions at both A- and B-sites. In theory, the tetrahedral and octahedral sites of inverse spinel originate the Fe^{+3} ions' magnetic moments in the AF-coupled system, and these magnetic moments cancel each other. Therefore, the Ni^{+2} ions are responsible for magnetization on the octahedral sites with moments of about 2 μB/fu [20–22]. As far as NFO is concerned, the properties of this material are stated to be greatly governed by the Fe and Ni cation distribution between A- and B-sites; the two are functions of the dopant levels and the sample preparation techniques.

Over the last few years, prediction of spectroscopic characteristics of distinct molecular geometries through full-scale energy calculation techniques has attracted great interest. These calculations are founded on time-dependent density functional theory (TD-DFT), whereby different simulation methods include DMol3 and CASTEP techniques [23, 24]. Previously, the Density Functional Theory (DFT) was used to investigate magneto-crystalline anisotropy. LSDA and GGA within the DFT were used to perform structural and electronic analysis for NFO [25, 26]. When it comes to more comparative simulations, some previous researchers have given the magnetic moments of NFO, density of states (DOS), and electronic spin-density functional-based energy bands. Moreover, electronic characteristics using X-ray absorption, magnetic circular dichroism spectra, and completely relativistic DIRAC LMTO with LSDA and LSDA + U formalism [27, 28].

The magnetic, morphological, and structural properties of prepared material are also based upon temperature and separation techniques during preparation [29]. Many approaches are applied to prepare nano-crystallite AB_2O_4. Some of them are named as sol–gel method [30, 31], co-precipitation, chemical reduction [32, 33], seeding, a microwave-assisted method, sono-electro-deposition, combustion method, solid-state method, solvent-deficient method [34, 35], the method of inert gas condensation, laser ablations, sputtering, ultrasound method, template synthesis, spark discharge, biological synthesis, hydrothermal method [36, 37], solvothermal method, microemulsion, and inverse microemulsion are the methods to prepare nanoparticles [].

The project refers to a cost-effective path to prepare nanoparticles of $NiFe_2O_4$ by applying the sol–gel auto-combustion method. After studying this ferrite using different experimental techniques, it has been found from the results that a single-phase sample can be synthesized at relatively lower temperatures [38, 39]. It was affirmed that single-phase formation is a prerequisite to use this material for a particular application. This is because if a sample contains impurities, then the impurities can deteriorate the performance of the material used for a particular application. In addition, in magnetic measurements, it can be seen that $NiFe_2O_4$ exhibits excellent magnetic properties when compared with the previous studies [2]. For example, it exhibits a saturation magnetization of 62 emu/g and a coercivity of 252 Oe in pure form, which are higher than the previously reported studies [40–42]. Such higher values are very suitable for high-frequency applications like microwave devices where high saturation magnetization and coercivity of a few hundred oersteds are desirable.

2 Synthesis procedure

The sol–gel method involves a wet-chemical process where precursors, typically metal alkoxides, undergo hydrolysis and condensation reactions to form a sol, which then transforms into a gel. This process is used to create various materials, including nanoparticles and thin films, with a degree of control over structure and properties [43–45]. The sol–gel route was applied to synthesize nanoparticles of nickel ferrites. All the chemicals used in the synthesis of nickel ferrites are from Sigma Aldrich of analytical grade taken from the laboratory, which are used without further purification. The nanoparticles of nickel ferrites were prepared using iron (III) nitrate nonahydrate and nickel (II) nitrate hexahydrate. First of all, 0.1 mol and 0.2 mol of nickel (II) nitrate hexahydrate ($m = 2.91$ g) and iron (III) nitrate nonahydrate ($m = 8.08$ g), respectively, were dissolved in 100 ml of D.I. water separately and stirred for about 30 min at room temperature to make a homogeneous solution. After that, both the salts are mixed and stirred for about 1 h. Citric acid is used in the ratio 1:1 as a chelating agent. The pH of the solution was maintained at 8 using an appropriate quantity of ammonia solution (NH_4OH). At 80 °C, the solution was stirred constantly for about 12 h so that the excess water evaporated and the solution transformed into viscous gel. The gel was viscous and brown. The gel is further transformed into a hot air oven for further drying. The temperature of the hot air oven is set for about 3 h. A puffy solid remains and, using a mortar and pestle, is ground into a fine powder. Finally, the prepared material is heated at 600 °C for 5 h in a muffle furnace, and the material is further ground. The following characterization techniques were applied to investigate the properties of prepared samples. X-ray diffraction technique was applied to investigate the underlying crystal structure of the prepared material by Cu-Kα (Mini Flex-III) with a wavelength of 1.54 Å and accelerating voltage 40 kV. SEM (Hitachi SU 1510 machine) was used to observe and analyze the surface morphology of prepared samples. The chemical bonds and functional groups of the prepared material were investigated through FT-IR. Shimadzu 8400S IR spectrometer recorded Infrared (IR) spectra by KBr pellets method. RAMAN spectroscope (Model: In Via Raman Microscope by RENISHAW UK, Excitation laser: 488-nm Laser Exposure time/s: 10 s, grating: 1800 I/mm, objective: X50L, laser power: 100%). VSM (Lakeshore-7407 with applied magnetic field ± 10,000 Oe and at room temperature) was applied for measuring a magnetic property of materials when it vibrated perpendicularly to uniform magnetic fields. High-frequency (up to 3 GHz) dielectric properties were measured using R & S ZVA. X-ray photoelectron spectroscopy (XPS, ESCA Lab MK II using non-monochromatized Mg Ka X-ray beams) was used to evaluate the presence of elements for the synthesis of $NiFe_2O_4$.

3 Results and discussion

3.1 Structural parameters

3.1.1 X-ray diffraction analysis

The structure of prepared nickel ferrites was depicted using Cu ray of wavelength 1.540593 Å in the width of 2θ degrees, which is illustrated in Fig. 1. The planes (111), (220), (311), (222), (400), (422), (511), and (440) show that the prepared material has a cubic structure that is in accordance with JCPDS card number 000-003-0875 []. The prepared material has a single phase because XRD patterns show no extra peaks. This means that the prepared material has no impurities. Various features of the prepared material were investigated, which are discussed below. The unit cell software (Jade6.5) was used to find the lattice constant (a) among the lattice planes of the crystal. To calculate the various structural parameters, the following formulas were used:

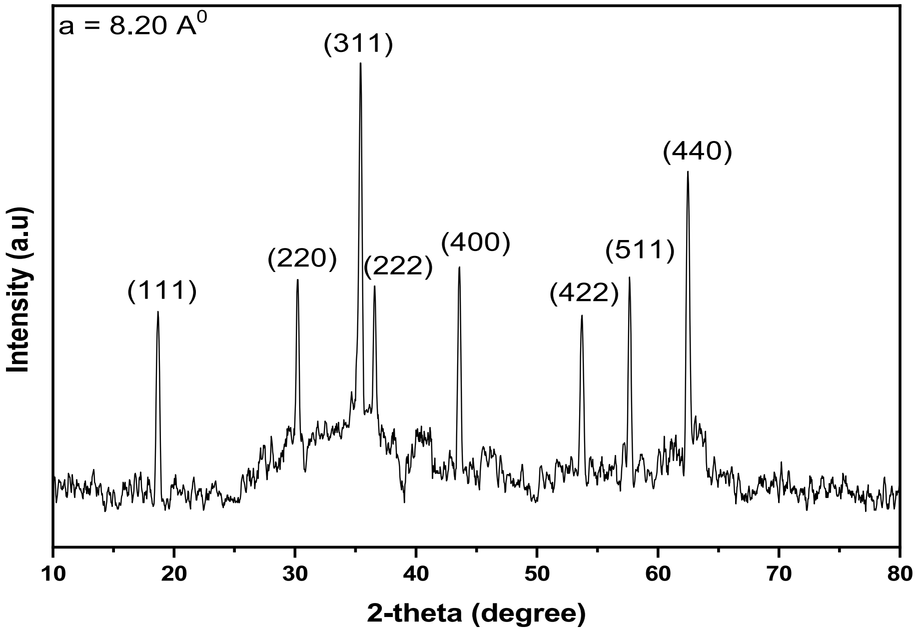

Fig. 1 XRD pattern of nickel ferrite ($NiFe_2O_4$)

The theoretical lattice constant is estimated by the following equation [46]:

$$a_{theo} = \frac{8}{3\sqrt{3}}\left[\left(r_A + R_o\right) + \sqrt{3}\left(r_B + R_o\right)\right] \tag{1}$$

The similarities were found between experimental and theoretical results.

The Scherrer formula is applied to find crystallite size [47, 48]:

$$D = \frac{K\lambda}{\beta\cos\theta} \tag{2}$$

In this expression, the crystallite size is represented by D, the Scherrer constant is denoted by K having a value of 0.9, where λ is the radiation wavelength (1.540593 Å), β represents the intense peaks full width at half-maximum (FWHM) (200), and Bragg's angle is indicated by (θ) [49].

The volume of the unit cell is estimated using the relation of the lattice constant as given below [50];

$$V = a^3 \tag{3}$$

X-ray density is estimated by applying the following relation [51];

$$D_x = \frac{N \times M}{N_A V} \tag{4}$$

In this expression, N is the effective number of atoms in a unit cell of cubic inverse spinel structure that is equal to 8, where M is the molecular weight having a value of V, V is the unit cell volume, and N_A is the Avogadro's number. All computed values of parameters are listed in Table 1. It can be observed that the values of all these parameters greatly match the earlier reported values for the same type of ferrite.

Table 1 Values of structural parameters of nickel ferrite $(NiFe_2O_4)$

a_{exp} (Å)	a_{theo} (Å)	D (nm)	V ($Å^3$)	D_x (gcm^{-3})
8.20	8.20	27	551.368	5.21

3.1.2 Inter-ionic distances and bond angles

The separation (b, c, d, e, f) among cation to cation (Me–Me) and distances (p, q, r, s) between cation and anion (Me–O) are shown in Fig. 2. The following formulae are used for their determination [52, 53].

$$p = \left(\frac{5}{8} - u\right)a \tag{5}$$

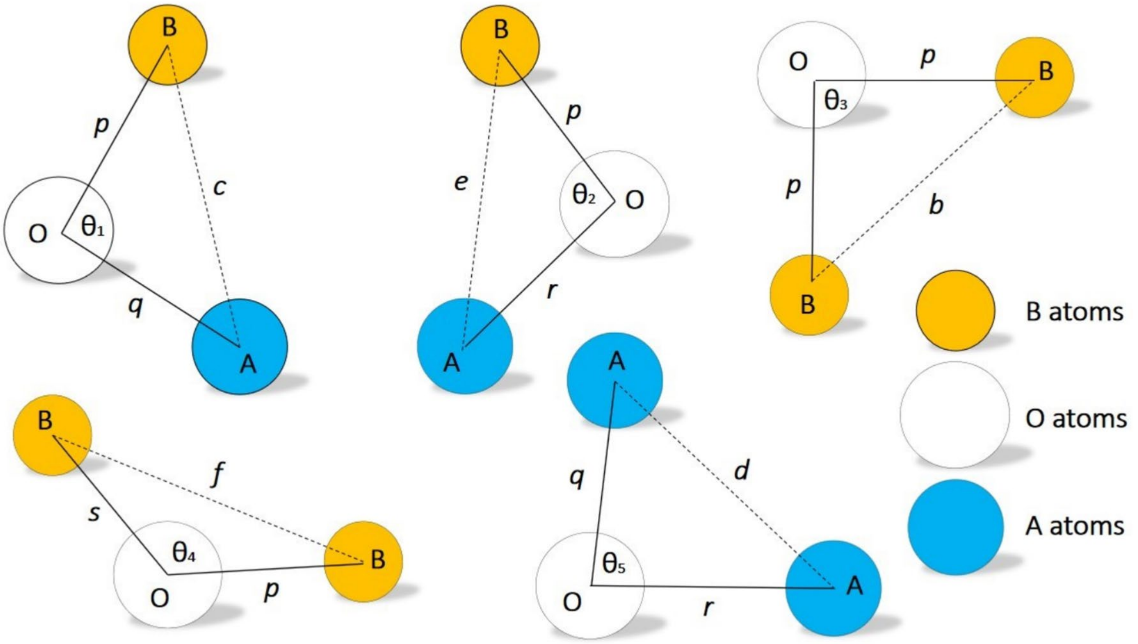

Fig. 2 Inter-ionic distances and bond angles illustration

$$q = \left(u - \frac{1}{4}\right)a\sqrt{3} \tag{6}$$

$$r = \left(u - \frac{1}{4}\right)a\sqrt{11} \tag{7}$$

$$s = \frac{a}{\sqrt{3}}\left(u + \frac{3}{8}\right) \tag{8}$$

$$b = \frac{\sqrt{2}}{4}a \tag{9}$$

$$c = \frac{\sqrt{11}}{8}a \tag{10}$$

$$d = \frac{\sqrt{3}}{4}a \tag{11}$$

$$e = \frac{3\sqrt{3}}{8}a \tag{12}$$

$$f = \frac{\sqrt{6}}{4}a \tag{13}$$

These calculated values are tabulated in Table 2.

The inter-ionic bond angles are estimated using the following relations [54, 55] and the calculated values are given in Table 3 which are in good agreement with the earlier reported literature [43]:

$$\theta_1 = \cos^{-1}\left(\frac{p^2 + q^2 - c^2}{2pq}\right) \tag{14}$$

$$\theta_2 = \cos^{-1}\left(\frac{p^2 + r^2 - e^2}{2pr}\right) \tag{15}$$

$$\theta_3 = \cos^{-1}\left(\frac{2p^2 - b^2}{2p^2}\right) \tag{16}$$

Table 3 Inter-ionic bond angles $(\theta_1, \theta_2, \theta_3, \theta_4, \theta_5)$ values for nickel ferrite $(NiFe_2O_4)$

θ_1(degree)	θ_2(degree)	θ_3(degree)	θ_4(degree)	θ_5(degree)
123.3400	144.9468	92.8536	125.9180	74.4807

$$\theta_4 = \cos^{-1}\left(\frac{p^2 + s^2 - f^2}{2ps}\right) \tag{17}$$

$$\theta_5 = \cos^{-1}\left(\frac{r^2 + q^2 - d^2}{2rq}\right) \tag{18}$$

3.1.3 *Tetrahedral and octahedral structural parameters*

The following relations were used to compute other parameters at A- and B-sites [56, 57], involving ionic radius (r_A & r_B), inter-ionic and cationic–anionic separations (R_A & R_B), bond length (d_{AL} & d_{BL}), hopping length (L_A & L_B), shared edge length (d_{ALE} & d_{BLE}), and unshared edge length (d_{BLEU}).

$$r_A = \left(u - \frac{1}{4}\right)a\sqrt{3} - R_o \tag{19}$$

$$r_B = \left(\frac{5}{8} - u\right)a - R_o \tag{20}$$

$$R_A = a\sqrt{3}\left(\delta + \frac{1}{8}\right) \tag{21}$$

$$R_B = a\sqrt{\left(\frac{1}{16} - \frac{\delta}{2} + 3\delta^2\right)} \tag{22}$$

$$L_A = \frac{1}{4}a\sqrt{3} \tag{23}$$

$$L_B = \frac{1}{4}a\sqrt{2} \tag{24}$$

$$d_{AL} = a\sqrt{3(u - 0.25)} \tag{25}$$

Table 2 Inter-ionic distances (p, q, r, s, b, c, d, e, f) values for nickel ferrite $(NiFe_2O_4)$

p (Å)	q (Å)	r (Å)	s (Å)	b (Å)	c (Å)	d (Å)	e (Å)	f (Å)
2.0008	1.8605	3.5627	3.5791	2.8991	3.3995	3.5507	5.3260	5.0214

$$d_{BL} = a\left(\sqrt{3u^2 - \frac{11}{4}u + \frac{43}{64}}\right) \tag{26}$$

$$d_{ALE} = a\sqrt{2}\left(2u - \frac{1}{2}\right) \tag{27}$$

$$d_{BLE} = a\sqrt{2}(1 - 2u) \tag{28}$$

$$d_{BLEU} = a\left(\sqrt{4u^2 - 3u + \frac{11}{16}}\right) \tag{29}$$

where $u = 0.381$ is the normal positioning characteristic of the oxygen ion and $R_o = 1.32$ Å is its radius for metal oxides. Regarding the FCC structure, $u_{ideal} = 0.375$ is considered best, and the deviation of the oxygen parameter is calculated using the formula $\delta = u - u_{ideal}$. The calculated values for each of these parameters are displayed in Table 4. The octahedral B and tetrahedral A sites comprise the FCC structure [58].

3.1.4 Theoretical calculations of structural properties using DFT

The structure of Nickel ferrite is generated using DFT inside the (FP-LAPW) method which was employed in the CASTEP [59]. It is noted that NFO has FCC structures with fd3m space group. The inverse spinal structure as generated in the CASTEP code is given in Fig. 3.

It has cubic unit cell consist of 56 atoms, in which oxygen atom occupy 32 atomic positions, Ni atom occupy 8 and the remaining 16 by the Fe atom. Fcc inverse spinel structure was calculated theoretically having lattice constant 8.20 A° and unit cell volume 580.0937 with space group fd-3 m (227). Fe^{3+} equally occupied by the octahedral and tetrahedral sites. N_i^{2+} occupies only octahedral sites and half of the octahedral sites are distributed by Fe^{3+} and the other half by N_i^{2+}.

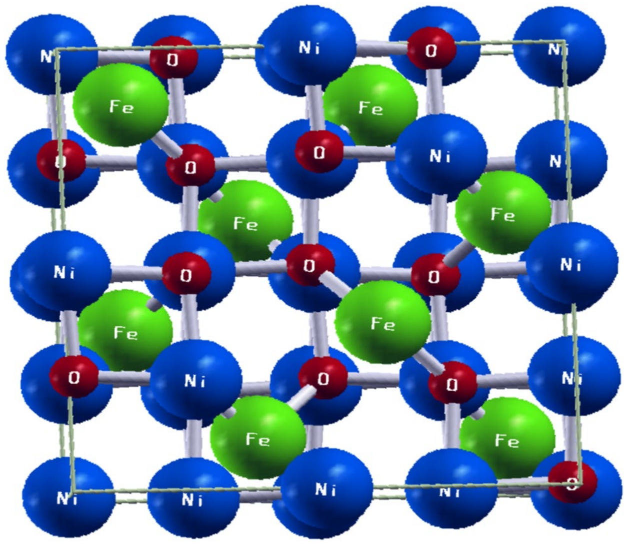

Fig. 3 Crystal Structure of Nickel Ferrite generated using DFT

3.1.5 Geometry optimization

To obtain the appropriate energy based upon volume, whole system energy is reduced to reach the ground state energy of the system. There are two processes that must be completed before this energy may be used. The interior forces exerted on one another inside the unit cell are estimated in the first phase. As a result, forces become insignificant in this phase, and the parameter u is decreased. Where in the 2nd phase, after choosing the c/a ratio, the curve between the energy and volume is optimized. We can achieve this using a Birch–Murnaghan equation, which allows us to compute the ground state parameters [44, 60, 61].

$$E(V) - E(V_o) = \left(\frac{B_oV}{B_o\prime}\right)\left[\frac{\left(\frac{V_o}{V}\right)^{B_o\prime}}{B_o} + 1\right] - \left[\frac{B_oV}{B_o\prime}\right] \tag{30}$$

Here,

- E(V) E_g with unit cell volume V
- E (V_o) E_g at zero pressure
- B_o bulk modulus
- $B_o\prime$ derivative of B_o at zero pressure

As a result, E_{total} is optimized at a certain volume that is called optimized volume.

Table 4 Tetrahedral and octahedral site values for nickel ferrite $(NiFe_2O_4)$

r_A (Å)	r_B (Å)	R_A (Å)	R_B (Å)	L_A (Å)	L_B (Å)	d_{AL} (Å)	d_{BL} (Å)	d_{ALE} (Å)	d_{BLE} (Å)	d_{BLEU} (Å)
0.5405	0.6808	1.8605	2.0020	3.5507	2.8991	5.1405	2.0020	3.0382	2.7599	2.9008

3.2 SEM analysis

Scanning Electron Microscopy (SEM) was applied to observe the morphology of nanoparticles as illustrated in Fig. 4 (a). These micrographs indicate that the particles are of varying sizes and non-uniform shapes with agglomeration in nanoparticles. The agglomeration is inhomogeneous. The surface has a non-uniform distribution of material. The grain size obeys the crystallite size trend, and magnitude varies because grains are made of crystallites. Figure 4(b–d) reflects the elemental mapping images (EMI) of $NiFe_2O_4$ ferrite, which were obtained to examine the distribution of different elements present in $NiFe_2O_4$ ferrite. The EMI images showed that the Ni, Fe, and O were homogeneously distributed in the ferrite sample, thereby confirming that the sample exhibits a single-phase spinel structure.

3.3 FT-IR analysis

FT-IR of nickel ferrite oxide ($NiFe_2O_4$) is shown in Fig. 5. The transmittance characteristic of the nickel ferrites oxide fine particles has been observed within range of $400 - 4000\ cm^{-1}$. The kind and nature of chemical bonding among metals ions and some other constituents in ferrites may be seen via infrared spectroscopy [29]. The water molecules absorption of samples observed at $3410\ cm^{-1}$ [58]. The samples are also show the absorbance at1632 cm^{-1} because of nitrate ions absorbance in the samples. It is clear from the graph that $NiFe_2O_4$ powder has absorbance peak at $598\ cm^{-1}$. The stretching vibrations are fundamental absorption bands at the octahedral and tetrahedral sites for inverse spinel ferrite [62]. The octahedral vibration, on the other hand, are not noticeable in this sample since they typically arise between $300\ cm^{-1}$ and $600\ cm^{-1}$ [29]. There are two clear metal–oxygen band at the value of $3410\ cm^{-1}$ and $598\ cm^{-1}$ are generally because of vibrations of ions existing within the crystals. The tetrahedral vibrations

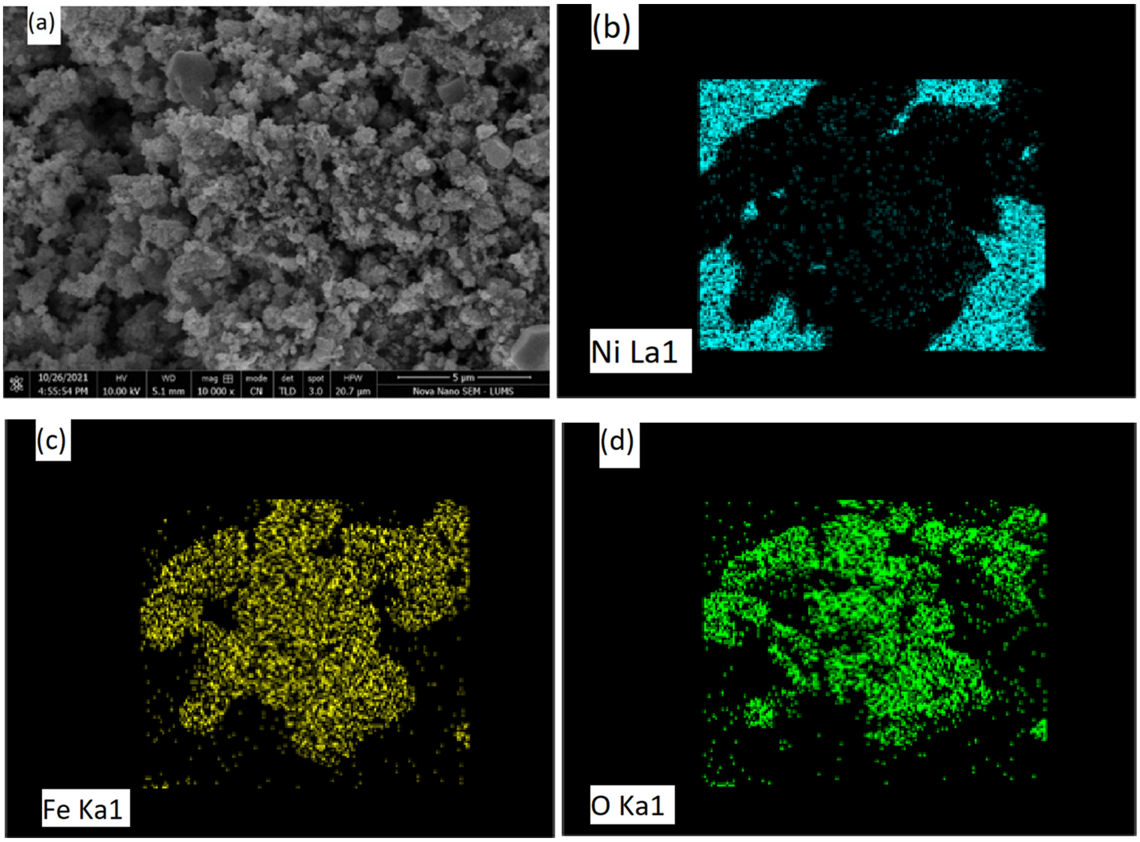

Fig. 4 **a** SEM image of nickel ferrite ($NiFe_2O_4$). **b–d** Elemental mapping images of $NiFe_2O_4$

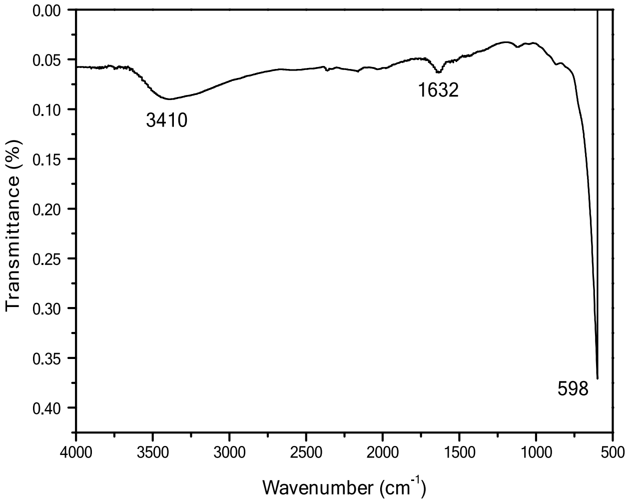

Fig. 5 FT-IR spectrum of nickel ferrite $\left(NiFe_2O_4\right)$

Table 5 Values of V_t, μ, and K_t for nickel ferrite $\left(NiFe_2O_4\right)$

$V_t\left(cm^{-1}\right)$	$\mu\times10^{-23}$(g)	$K_t\times10^{5}$(dyne/cm)
598	3.9901	5.0627

(V_t) were found from Fig. 5, and force constants (K_t) are calculated using Eq. 30 [63].

$$K_t = 4\pi^2V_t^2c^2\mu \tag{31}$$

$$\frac{1}{\mu} = \frac{1}{m_1} + \frac{1}{m_2} + \frac{1}{m_3} + \dots \tag{32}$$

where (V_t) is 598 cm^{-1}, speed of light (c) is $2.99972458 \times 10^{10} cms^{-1}$, and mass reduction (μ) is estimated by Eq. 31 [64, 65] for tetrahedral sites. The results are shown in Table 5.

3.4 Electronic properties

The electronic properties are basically revealed from the band structure of the compound.

3.4.1 *Band structure*

Significant proof regarding the substance is interpreted using the band structure that may be direct or indirect. It also tells about the energy range for the electrons within the solids that may have an energy band or may not. The electronic band structure for NFO is computed with several symmetric points in the 1st Brillouin zone which were employed in PBE-GGA (Fig. 6).

According to the band structure of the sample, both spin-up and spin-down channels cross the Fermi level, but there is a difference of 2.5 eV between the valence and conduction bands, which confirms that the compound is half metal.

3.4.2 *Density of states*

In nickel ferrite, the DOS is computed as shown in Fig. 7. The computed DOS at 0.4 and 1.3 demonstrates

Fig. 6 Band structure for Nickel Ferrite

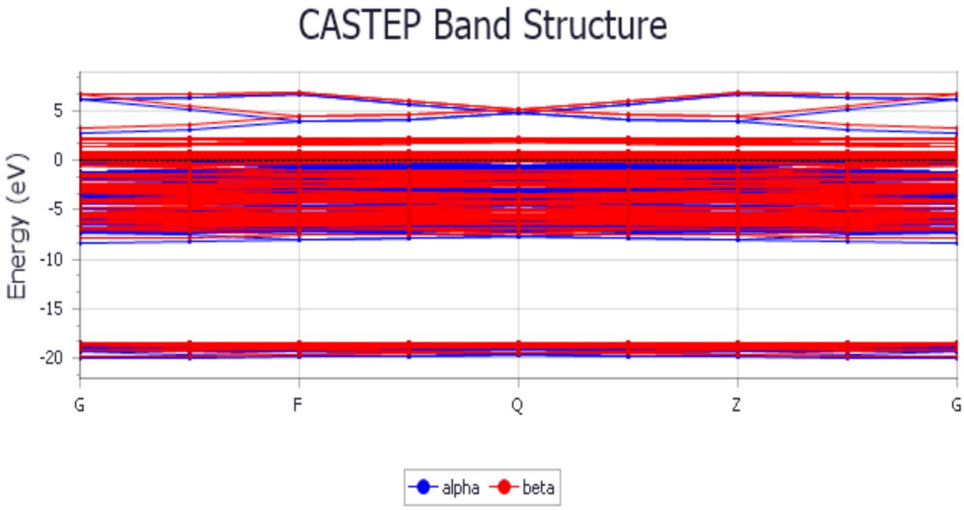

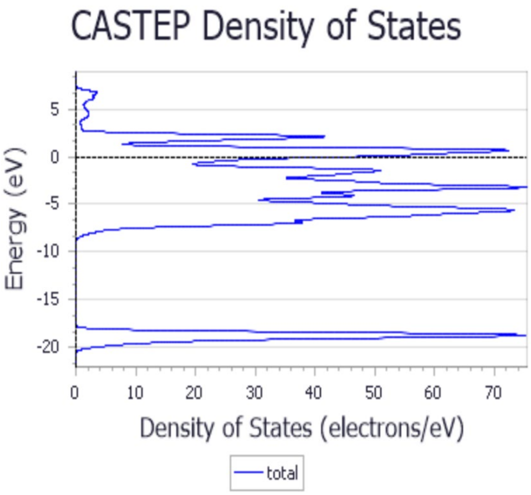

Fig. 7 Density of states for Nickel Ferrite

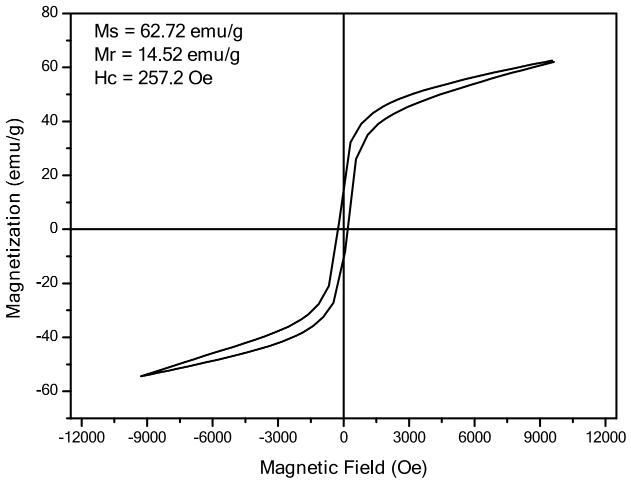

Fig. 8 M − H loop of nickel ferrite $(NiFe_2O_4)$

that nickel ferrite is a semi-metal, where the value of the band gap was about 2.5 eV. The intra-site Coulomb repulsion of and as calculated from DOS was observed to be 10 eV and 12 eV, respectively, which were too close to the experimental results. From DOS, it was revealed that lower Hubbard bands were lower than the O bands. This demonstrates the ability to transfer large amounts of charge. On the other hand, lower Hubbard bands interact strongly with the O bands. The crystal area of site B is clearly greater than that of site A, as anticipated by crystal field theory, based on the Fe^{3+} split. There are both spin-up and spin-down alignments. According to spin-down alignments, it crosses the Fermi level and indicates the conducting nature of Fe, but spin-up alignment shows that there is an energy band gap of 2 eV, showing the half-metal nature of the sample.

3.5 Magnetic properties

For the investigation of the magnetic properties of the loop, a plot was made at room temperature using the VSM technique. Several parameters about magnetic properties were found through loops, like remanence, saturation magnetization, and coercivity. The loop is shown in Fig. 8, revealing the ferromagnetic nature of the prepared material. The small hysteresis loop area indicates that the prepared material is a soft ferrite. The intrinsic and extrinsic factors, such as lattice strain, lattice parameters, cation distribution and density, route of preparation, and structure, respectively, significantly impact the magnetic characteristics of the material [66].

Different magnetic parameters such as coercivity, saturation magnetization (Ms), and remanence (Mr) were obtained from the loops, as shown in Table 6. It is obvious from these values that the synthesized nickel ferrite exhibits excellent magnetic properties and shows soft magnetic behavior, thereby confirming that the material can be used for different technological applications such as transformer cores, recording media, high-frequency devices, and dielectric resonators. The magnetic moment was calculated using Eq. 33 [67]. The octahedral site is occupied by and both and are resident in tetrahedral sites in inverse spinel nickel ferrites, and thus the total magnetic moment is in good accord with the experimental values [68]:

$$n_B(\mu_B) = \frac{M \times M_S}{5585} \tag{33}$$

In this expression, molecular weights and saturation magnetization are represented by M and Ms, respectively.

The Mr /Ms ratio is known as the squareness ratio. Table 6 shows the small squareness value that indicates that the material contains multi-domain grains. Also, we can calculate the anisotropic constant as well as the anisotropic fields by Eqs. 34 and 35 [69, 70].

$$K = \frac{H_s \times M_s}{0.96} \tag{34}$$

Table 6 Magnetic properties of nickel ferrite $\left(NiFe_2O_4\right)$

Ms(emu/g)	Ms (LOA)(emu/g)	Mr(emu/g)	Mr/Ms	$n_B\,(\mu_B)$	H_C	K (erg/g)	H_K (10^7)
62.72	62.97	14.52	0.2315	2.63	257.2	16,803	42

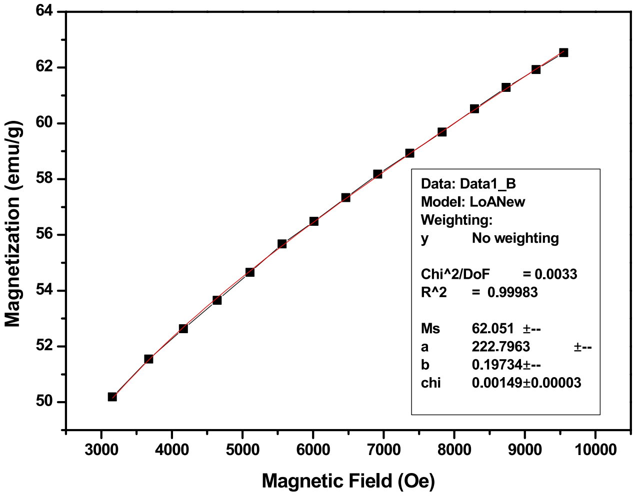

Fig. 9 Fitted curves using the M – H loop data of nickel ferrite $\left(NiFe_2O_4\right)$

$$H_k = \frac{2K}{\mu_\circ M_S} \tag{35}$$

where H_C is the coercivity, M_S is the saturation magnetization, and the value of $\mu_\circ$ is $4\pi \times 10^{-7} H/m$. The grains size has an indirect relationship with coercivity [71]. As grain size is decreased, the grain boundary is increased, make difficult to align the domains [72]. The law of approach (LOA) was utilized to determine the saturation magnetization (M_S) maximum value which was 62.051 emu/g as shown in Fig. 9. The following equation was used that relates magnetization (M) to maximum applied magnetic field (H) [58, 73].

$$M = M_S\left(1M - \frac{A}{H} - \frac{B}{H^2}\right) + \chi H \tag{36}$$

The above-mentioned parameters such as Ms represents saturation magnetization, assuming that the Brillouin function is equal to unity, A represents inhomogeneities present in the sample, B is proportional to K^2 (where K is the anisotropic constant), H is the applied magnetic field, and χ is the magnetic susceptibility.

3.6 Magnetic properties using DFT

For the estimation of magnetic properties of NFO, we simply focused on the atomic total spin arrangement, rather than the precise valence electronic structure. Only the resultant local magnetic moment for each metallic species will be examined and this may be spin up (↑) or spin down (↓). We know that for inverse spinel NFO, Fe atoms are present at two positions that may be octahedral or tetrahedral, that's why they have to treat separately (Fig. 10). As a result, a greater number of initial total spin configurations have been considered. In ferromagnetic materials total magnetic moments are aligned and parallel (i.e., spin up ↑ for both Ni (T_d) and Fe (O_h) but this structure is ferrimagnetic in which Ni^{2+} and Fe^{3+} having anti-parallel magnetic moments (i.e., ↑ for $Ni(T_d)$ and ↓ for $Fe(O_h)$).

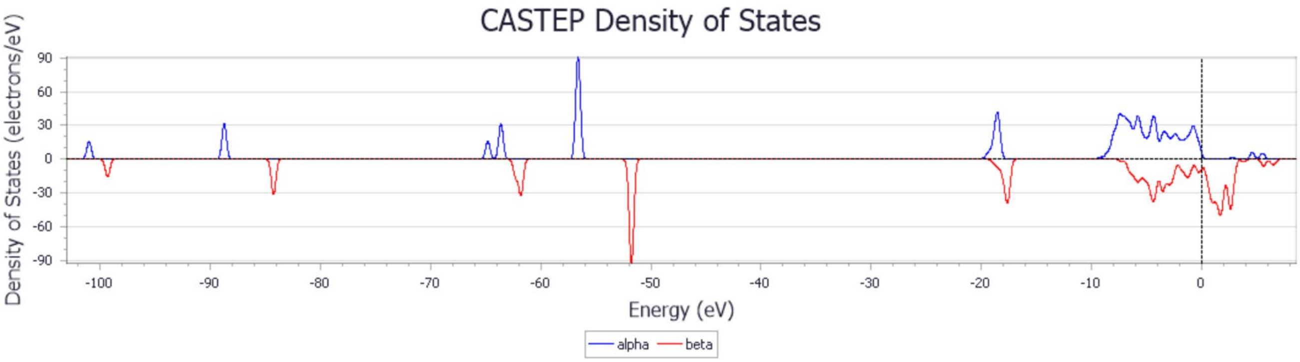

Fig. 10 Spin-up and Spin-down alignment for magnetic properties of Nickel Ferrite

For Ni (Oh) | Fe (Td) |Fe(Oh) having ↑↓↑ magnetic moment arrangement. In present structure both Fe atoms which are at octahedral and tetrahedral sites having anti-parallel moments and cancel the effect of each other. As a result, the overall magnetic moments present in the structures are due to presence of Ni (Oh) atoms. The local magnetic moments were calculated as 4|4|2|0 μ_B for Ni (Oh) |Fe (Td)|Fe(Oh)|O on the atoms separately. The net magnetic moment on the whole structure was found to be 2.5 μ_B which is comparatively close to the experimental value that's 2.63 μ_B.The crystal of NFO comprising of 2 magnetic sub lattices, which are due to Fe^{3+} and 2nd one Ni^{2+} with initial magnetic moment of 4 $\mu_B(d^5)$ and 2 $\mu_B(d^8)$.

3.7 High-frequency dielectric properties

The dielectric constant and dielectric loss as a function of frequency (up to 3 GHz) are shown in Fig. 11 (a and b). With the increase in the value of the applied frequency, the value of the dielectric constant decreases. This behavior of ferrites in common can be explained as follows: the general form of spinel ferrites is represented by AB_2O_4, where A and B are tetrahedral and octahedral sites, respectively. The electrons hopping at the octahedral B-sites between Fe^{3+} and Fe^{2+} are responsible for conduction in ferrites [74].

$$Fe^{3+} + 1e^- \leftrightarrow Fe^{2+} \tag{37}$$

The theory of Maxwell, Wagner, and Koop states that conduction shows a key role among the charges hopping and electrons [75]. The ferrites have two major layers: conducting grains and extremely resistant grain boundaries. There is negligible interfacial polarization at high frequencies of more than 100 kHz. Atomic and electronic polarizations are effective in a range of more than 10 MHz. This polarization is similar to electron movement between Fe^{2+} and Fe^{3+} ions. The electron exchange is efficient at low frequency, which leads to a high dielectric constant. Nevertheless, the electron exchange becomes less efficient as frequency increases, which causes the dielectric constant to decrease [76, 77]. Moreover, Fig. 11 (a and b) also shows how dielectric constant and loss vary with frequency at different temperatures (300 K, 325 K, and 350 K), and it includes the variation at various frequencies for dielectric loss as well as dielectric constant.

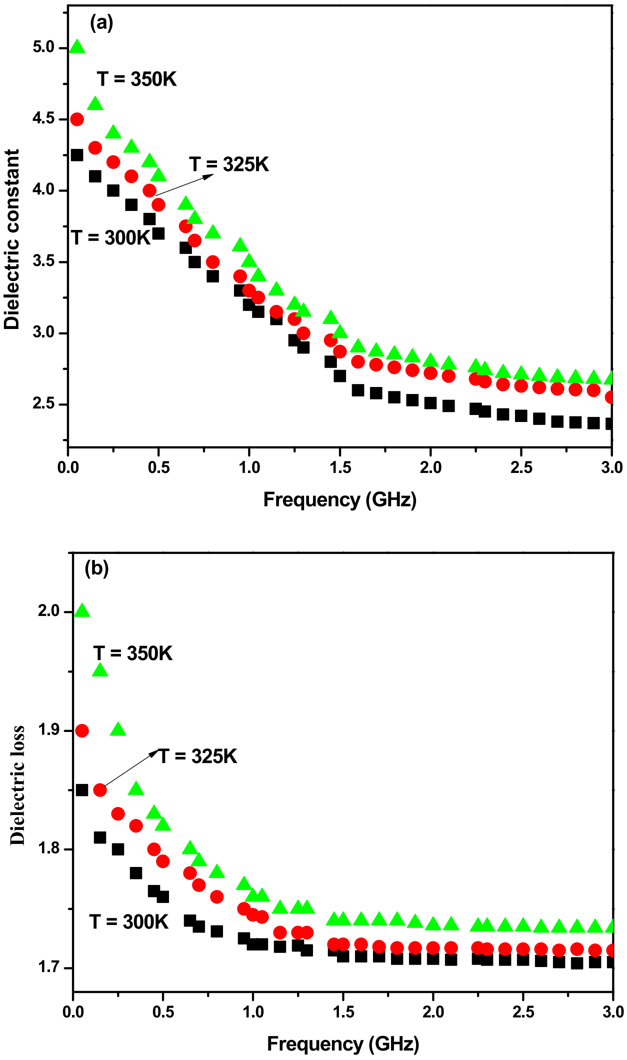

Fig. 11 Variation of **a** dielectric constant and **b** dielectric loss as a function of frequency at different temperatures

3.7.1 *Dielectric constant and dielectric loss with varying temperature*

The variation in both dielectric constant and dielectric loss with increasing temperature (300–350 K) at different high frequencies (10 MHz, 1 GHz, and 3 GHz) is reflected in Fig. 12 (a and b). The increase in temperature causes the increase in both parameters. The increase is relatively prominent at low frequency and high temperature. The charge carriers between Fe^{3+} and Fe^{2+} are thermally activated, which increases the carriers' exchange interactions; hence, an increase in the values of the dielectric constant is observed. It has been reported in earlier literature that dipolar and interfacial polarization are significant and mainly

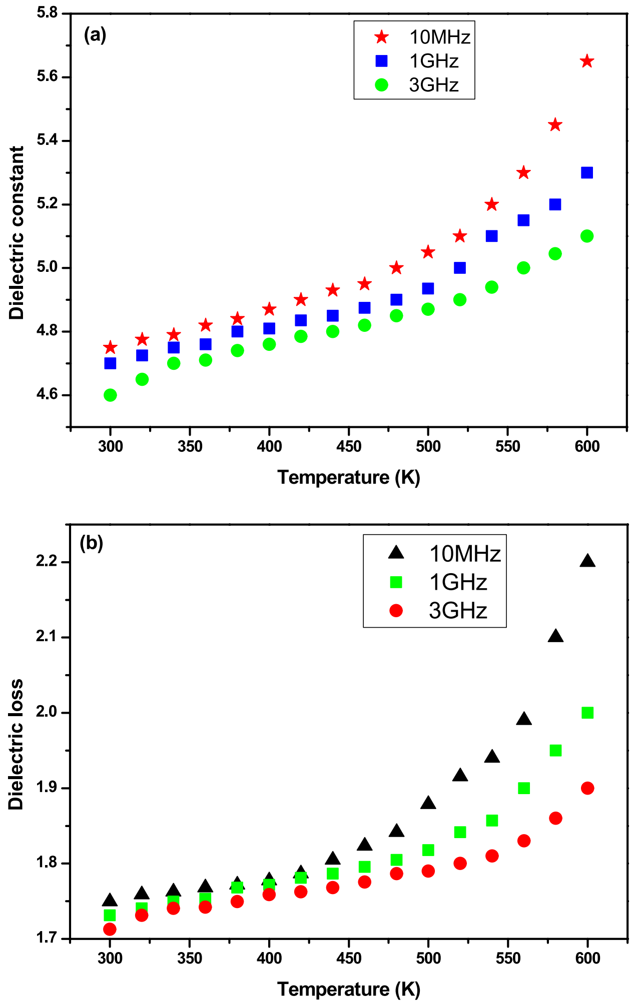

Fig. 12 Variation of **a** dielectric constant and **b** dielectric loss as a function of temperature at different frequencies

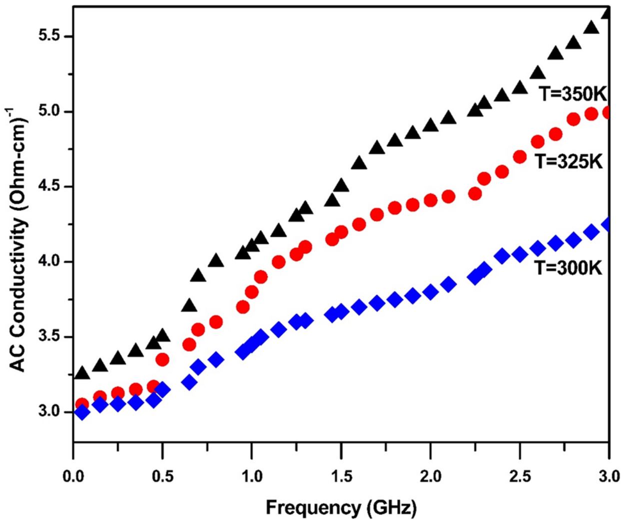

Fig. 13 Variation of AC conductivity as a function of frequency at different temperatures

depend upon temperature. Interfacial polarization increases, whereas dipolar polarization decreases with increasing temperature [78]. Interfacial polarization is mostly responsible for the increase in dielectric constant values for the frequency values. Ferrites' dielectric constant is comparable to the conducting phenomena that result from the charge carriers shifting from Fe^{3+} to Fe^{2+} in the direction of the applied field. The polarization has been significantly influenced by the observed displacement of electrons (n) and holes (p) charge carriers, which is temperature dependent. Therefore, the conductivity of spinal ferrites rises with temperature due to an increase in thermal activation and charge carrier mobility between Fe^{3+} and Fe^{2+} ions [79]. Resultantly, overall dielectric polarization increases, and hence an increase in both dielectric constant and dielectric loss is observed, as shown in Fig. 12 (a and b). Figure 13 refers to the AC conductivity as a function of frequency at different temperatures. The AC conductivity was calculated using the following equation and its variation with high frequency (10 MHz–3 GHz).

$$6_{AC} = \omega\epsilon_0\varepsilon\prime\tan\delta = \omega\epsilon_0\epsilon \quad (38)$$

Conducting processes in ferrite materials are caused by electrons (n) and holes (p) hopping between Fe^{3+} and Fe^{2+} ions at octahedral B-sites. Figure 13 shows that as the applied frequency increases, AC conductivity progressively rises [80]. AC conductivity rises as a result of the frequency increase because it raises the frequency of electrons and holes hopping between the Fe^{3+} and Fe^{2+} ions. According to Koop's phenomenological theory and the Maxwell–Wagner model, the conducting grains in spinal ferrites are thought to be separated by thin, extremely insulating grain boundaries [77]. According to the current study's observed results on AC conductivity, conducting grains exhibit a dominant role at higher frequencies, whereas grain boundaries play a dominant function at lower frequencies. Therefore, it can be confirmed that the AC conductivity of the studied ferrites is influenced by both conducting grains and extremely resistant grain boundaries [81]. The increase in these properties with temperature can be explained as follows.

At higher temperatures, thermal energy increases the mobility of dipolar species (such as Fe^{3+}–O^{2-}–Fe^{2+} pairs in ferrites). This allows dipoles to align more easily with the alternating electric field, thereby increasing the dielectric constant [74]. Also, in heterogeneous materials (like polycrystalline ferrites), grains are more conductive than grain boundaries. At higher temperatures, grain boundary resistivity decreases, enhancing interfacial charge accumulation, which contributes to a higher dielectric constant. With a temperature rise, thermally activated electrons or small polarons (e.g., $Fe^{2+} \leftrightarrow Fe^{3+}$ hopping) contribute to higher AC conductivity. This causes greater energy dissipation in the form of heat, which manifests as increased dielectric loss [76]. At high temperatures, dipoles may not keep up with the alternating field, leading to a phase lag. This phase difference between polarization and the electric field results in higher dielectric loss. Elevated temperatures reduce the barrier for charge carrier movement, increasing leakage currents. This further contributes to dielectric losses [77].

3.8 X-ray photoelectron spectroscopy (XPS) analysis

X-Ray Photo-spectroscopy (XPS) was used to examine the surface chemical composition properties and to confirm the single-phase formation of $NiFe_2O_4$ [82–84]. Figure 14a reflects the XPS wide scan spectrum patterns of Ni2p, Fe2p, and O1s, with the peaks observed in the wide-angle spectra. The presence of Ni^{2+} is ascertained in Fig. 14b with the binding energy and satellite peaks at 855 eV and 861 eV, respectively [85-87], attributed to Ni $2p_{3/2}$. Figure 14c shows the peaks located at 710 eV, with its satellite peak at 712 eV and an additional peak at 724 eV, with its satellite peak at 719 eV representing the $Fe2p_{3/2}$ and $Fe2p_{1/2}$ for Fe^{3+} state, respectively, to confirm that the valence state of iron is 3 [88-92]. Figure 14d shows the O1s spectrum that displays the peaks at

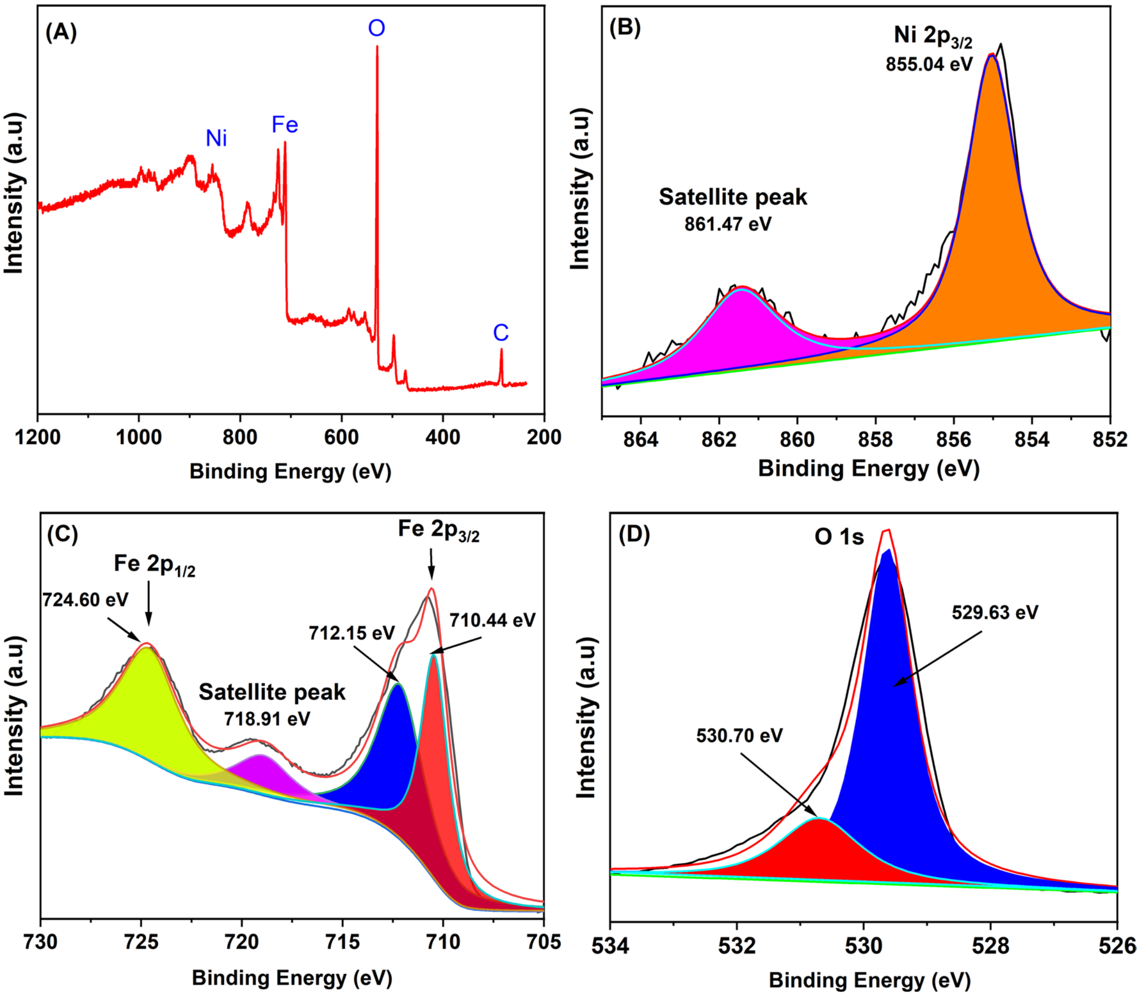

Fig. 14 **a** XPS wide scan spectrum of $NiFe_2O_4$. **b** Ni 2p spectra of $NiFe_2O_4$. **c** Fe 2p spectra of $NiFe_2O_4$, **d** O 1s XPS spectra of $NiFe_2O_4$

529 eV and 531 eV. The peak at 529 eV is allotted to O^{2-} ions, while the peak at 531 eV is allocated to O^{1-} ions present in the structure of $NiFe_2O_4$.

4 Conclusion

Single-phase nickel ferrite nanoparticles have been successfully synthesized using the sol–gel route. Several characterization methodologies were adopted to characterize the NFO. Theoretically, we adopted the Density Functional Theory (DFT) calculation using CASTEP code by employing generalized gradient approximation (GGA), local spin-density approximation (LSDA), and local density approximation (LDA) approximations. XRD showed the inverse spinel structures with lattice constant 8.20 Å, which is in good agreement with the theoretical value that is 8.20 Å at the optimized volume Vo. SEM analysis revealed the non-uniform distribution of particles with different sizes and the agglomeration. Because of octahedral sites existing within the structure, the absorption peak was observed at 598 cm^{-1}, confirmed by the FT-IR. VSM characterization confirms the soft ferrite nature of the nickel ferrite with a small M–H loop area and magnetic moment of 2.63, which was close to the DFT-calculated average value of 2.5, which made the sample best for microwave devices. The electronic nature of NFO was analyzed from band structure and density of states as generated from DFT calculations and comes out to be 2.5 eV, revealing the half-metallic nature of the material, thereby leading to the best one for high-frequency power cores. The theory of Maxwell, Wagner, and Koops is confirmed by the variation of dielectric properties with increasing frequency and temperature. Also, it was observed that the AC conductivity of the studied ferrites is influenced by both conducting grains and extremely resistant grain borders.

Acknowledgements

The authors would like to thank Princess Nourah bint Abdulrahman University Researchers Supporting Project number (PNURSP2025R316), Princess Nourah bint Abdulrahman University, Riyadh, Saudi Arabia.

Author contributions

The author Muhammad Asif helped to characterize and analyze the results of the samples; Wasif Irshad and Ghulam Abbas Ashraf wrote up the original draft; Muhammad Iqbal Asif, Atiq ur Rehman, Doniyor Jumanazarov, and Farruh Atamurotov edited the original draft; Mukhtar Ahmad supervised the project; and Yousef Mohammed Alanazi and Rizwan ul Hassan provided necessary experimental facilities.

Funding

The authors received no financial support for the research of this article.

Data availability

The relevant data supporting the findings of this study are available from the corresponding author upon reasonable request.

Declarations

Conflict of interest The authors declare that they have no conflict of interest regarding the publication of this article.

References

1. Najafi, M., H. Haratizadeh, and M. Ghezellou, 2015 *The effect of annealing, synthesis temperature and structure on photoluminescence properties of Eu-doped ZnO nanorods*.
2. M. Ahmadzadeh, M. Almasi-Kashi, A. Ramazani, CoFe layers thickness and annealing effect on the magnetic behavior of the CoFe/Cu multilayer nanowires. J. Nanostruct. **5**(2), 97–104 (2015)
3. F. Ghoreishi, V. Ahmadi, M. Samadpour, Synthesis and characterization of graphene-ZnO nanocomposite and its application in photovoltaic cells. J. Nanostruct. **3**(4), 453–459 (2013)
4. M. Salavati-Niasari, F. Davar, Z. Fereshteh, Synthesis of nickel and nickel oxide nanoparticles via heat-treatment of simple octanoate precursor. J. Alloys Compd. **494**(1–2), 410–414 (2010)

5. Z. Heydariyan et al., Facile preparation and characterization of $SmMn_2O_5/Mn_2O_3$/g-C3N4 nanocomposites for electrochemical hydrogen storage application. Int. J. Hydrogen Energy **90**, 1300–1312 (2024)
6. S. Akbar Hoseini, S. Khademolhoseini, Investigation of the structural, optical and magnetic properties of nickel ferrite nanoparticles synthesized through modified sol–gel method. J. Mater. Sci. Mater. Electron. **27**, 5943–5947 (2016)
7. M. Rahimi-Nasrabadi et al., Facile synthesis optimization and structure characterization of zinc tungstate nanoparticles. Mater. Manuf. Process. **30**(1), 34–40 (2015)
8. M. Rahimi-Nasrabadi et al., Electrosynthesis and characterization of zinc tungstate nanoparticles. J. Mol. Struct. **1047**, 31–36 (2013)
9. S. Moshtaghi, M. Salavati-Niasari, D. Ghanbari, Characterization of CaSn (OH) 6 and $CaSnO_3$ nanostructures synthesized by a new precursor. J. Nanostruct. **5**(2), 169–174 (2015)
10. Rahdar, A., M. Aliahmad, and Y. Azizi, 2015 *NiO nanoparticles: synthesis and characterization.*
11. SAFAEI, G.J., et al., 2015 *MgO nanoparticles: an efficient, green and reusable catalyst for the onepot syntheses of 2, 6-dicyanoanilines and 1, 3-diarylpropyl malononitriles under different conditions.*
12. I. Nlebedim et al., Effect of heat treatment on the magnetic and magnetoelastic properties of cobalt ferrite. J. Magn. Magn. Mater. **322**(14), 1929–1933 (2010)
13. Schmid, G., *Nanoparticles: from theory to application*. 2011: John Wiley & Sons.
14. F. Li et al., Stoichiometric synthesis of pure MFe_2O_4 (M= Mg Co, and Ni) spinel ferrites from tailored layered double hydroxide (hydrotalcite-like) precursors. Chem. Mater. **16**(8), 1597–1602 (2004)
15. Gharagozlou, M., 2009 *Synthesis and characterization of nanocrystalline magnetic pigment via coordinated precursors.*
16. S.B. Somvanshi et al., Hydrophobic to hydrophilic surface transformation of nano-scale zinc ferrite via oleic acid coating: magnetic hyperthermia study towards biomedical applications. Ceram. Int. **46**(6), 7642–7653 (2020)
17. S. Joshi et al., Structural, magnetic, dielectric and optical properties of nickel ferrite nanoparticles synthesized by co-precipitation method. J. Mol. Struct. **1076**, 55–62 (2014)
18. M. Khairy, M. Gouda, Electrical and optical properties of nickel ferrite/polyaniline nanocomposite. J. Adv. Res. **6**(4), 555–562 (2015)
19. R. Sharma, S. Singhal, Structural, magnetic and electrical properties of zinc doped nickel ferrite and their application in photo catalytic degradation of methylene blue. Physica B **414**, 83–90 (2013)
20. K. Pubby et al., Cobalt substituted nickel ferrites via Pechini's sol–gel citrate route: X-band electromagnetic characterization. J. Magn. Magn. Mater. **466**, 430–445 (2018)
21. K. Panwar et al., The effect of Cr substitution on the structural, electronic and magnetic properties of pulsed laser deposited $NiFe_2O_4$ thin films. J. Magn. Magn. Mater. **421**, 25–30 (2017)
22. U.-G. Jong et al., First-principles study of ferroelectricity induced by p–d hybridization in ferrimagnetic $NiFe_2O_4$. Phys. Lett. A **380**(40), 3302–3306 (2016)
23. S. Sayyah et al., Oxidative chemical polymerization, kinetic study, characterization and DFT calculations of para-toluidine in acid medium using $K_2Cr_2O_7$ as oxidizing agent. Int. J. Adv. Res. **3**, 266–287 (2015)
24. A.R. Ghazy et al., Synthesis, structural and optical properties of fungal biosynthesized Cu2O nanoparticles doped poly methyl methacrylate-co-acrylonitrile copolymer nanocomposite films using experimental data and TD-DFT/DMOl3 computations. J. Mol. Struct. **1269**, 133776 (2022)
25. C.J. O'Brien, Z. Rák, D.W. Brenner, Calculated stability and structure of nickel ferrite crystal surfaces in hydrothermal environments. J. Phys. Chem. C **118**(10), 5414–5423 (2014)
26. C. O'Brien, Z. Rák, D. Brenner, Free energies of (Co, Fe, Ni, Zn) Fe_2O_4 spinels and oxides in water at high temperatures and pressure from density functional theory: results for stoichiometric NiO and $NiFe_2O_4$ surfaces. J. Phys. Condens. Matter **25**(44), 445008 (2013)
27. A. Ghazy et al., Structure, optical properties, TD-DFT simulations for nanosecond and continuous laser irradiation of vanadium antimony borate glass doped with nickel ferrite. Sci. Rep. **14**(1), 89 (2024)
28. K. Panwar et al., Structural, magnetic and electronic properties of nickel ferrites: experiment and LCAO calculations. J. Alloys Compd. **831**, 154835 (2020)
29. ur Rehman et al., Evaluations of structural, magnetic and various dielectric parameters of Ni-substituted Zn2W-type hexagonal ferrites for high frequency (1–6 GHz) applications. Ceram. Int. **45**(18), 24202–24211 (2019)
30. X. Li et al., Influence of NbC particles on microstructure and mechanical properties of AlCoCrFeNi high-entropy alloy coatings prepared by laser cladding. J. Alloys Compd. **788**, 485–494 (2019)
31. N. Kaur, M. Kaur, Comparative studies on impact of synthesis methods on structural and magnetic properties of magnesium ferrite nanoparticles. Process. Appl. Ceram. **8**(3), 137–143 (2014)

32. J. Chandradass et al., Influence of processing methodology on the structural and magnetic behavior of $MgFe_2O_4$ nanopowders. J. Alloy. Compd. **517**, 164–169 (2012)
33. N.H. Nam, N.H. Luong, Nanoparticles: Synthesis and applications, in *Materials for biomedical engineering*. (Elsevier, 2019), pp.211–240
34. A.V. Rane et al., Methods for synthesis of nanoparticles and fabrication of nanocomposites, in *Synthesis of inorganic nanomaterials*. (Elsevier, 2018), pp.121–139
35. M.J. Uddin, Y.-K. Jeong, Adsorptive removal of pollutants from water using magnesium ferrite nanoadsorbent: a promising future material for water purification. Environ. Sci. Pollut. Res. **29**(7), 9422–9447 (2022)
36. K. Hachem et al., Methods of chemical synthesis in the synthesis of nanomaterial and nanoparticles by the chemical deposition method: a review. BioNanoScience **12**(3), 1032–1057 (2022)
37. C. Aoopngan et al., Amine-functionalized and hydroxyl-functionalized magnesium ferrite nanoparticles for Congo red adsorption. ACS Appl. Nano Mater. **2**(8), 5329–5341 (2019)
38. R. Monsef, M. Salavati-Niasari, Fundamental understanding on cyclability behaviors of ammonium vanadate nanoarchitectures as cathode materials for Li-ion batteries: a comparative insight of dual modification of precursor and morphology. J. Energy Storage **74**, 109395 (2023)
39. G. Kianpour, M. Salavati-Niasari, H. Emadi, Sonochemical synthesis and characterization of NiMoO4 nanorods. Ultrason. Sonochem. **20**(1), 418–424 (2013)
40. F. Mohandes, M. Salavati-Niasari, Sonochemical synthesis of silver vanadium oxide micro/nanorods: solvent and surfactant effects. Ultrason. Sonochem. **20**(1), 354–365 (2013)
41. M. Salavati-Niasari, M.R. Loghman-Estarki, F. Davar, Controllable synthesis of nanocrystalline CdS with different morphologies by hydrothermal process in the presence of thioglycolic acid. Chem. Eng. J. **145**(2), 346–350 (2008)
42. M. Salavati-Niasari, Zeolite-encapsulation copper (II) complexes with 14-membered hexaaza macrocycles: synthesis, characterization and catalytic activity. J. Mol. Catal. A Chem. **217**(1–2), 87–92 (2004)
43. M.W. Mukhtar et al., Synthesis and properties of Pr-substituted MgZn ferrites for core materials and high frequency applications. J. Magn. Magn. Mater. **381**, 173–178 (2015)
44. Batool, U., et al., 2025 *Impact of Rare Earth Cerium (Ce) Substitution on Structural, Magnetic and Electrochemical Properties of Lithium Ferrites: A Comprehensive Study.* Materials Chemistry and Physics. 130792.
45. N. AlMasoud et al., Sol-gel synthesis of Tb-doped lithium-nickel ferrite anchored onto g-C3N4 sheets for efficient photocatalytic degradation of organic dyes. Ceram. Int. **50**(22), 46892–46903 (2024)
46. N. Abu-Elsaad, Elastic properties of germanium substituted lithium ferrite. J. Mol. Struct. **1075**, 546–550 (2014)
47. M. Ajmal et al., The influence of Ga doping on structural magnetic and dielectric properties of NiCr0. 2Fe1. 8O4 spinel ferrite. Physica B **526**, 149–154 (2017)
48. M. Sithole et al., Visible light active gC 3 N 4 sheets/CdS heterojunction photocatalyst for decolourisation of acid blue (AB-25). J. Nanopart. Res. **23**, 1–17 (2021)
49. M.J. Iqbal, S. Farooq, Effect of doping of divalent and trivalent metal ions on the structural and electrical properties of magnesium aluminate. Mater. Sci. Eng., B **136**(2–3), 140–147 (2007)
50. A.A. Ati et al., Structural and magnetic properties of Co–Al substituted Ni ferrites synthesized by co-precipitation method. J. Mol. Struct. **1058**, 136–141 (2014)
51. M. Ahmad et al., Lithium ferrite (Li_0. $5Fe_2$. $5O_4$): synthesis, structural, morphological and magnetic evaluation for storage devices. J. Mater. Res. Technol. **18**, 3386–3395 (2022)
52. N. Vasoya et al., Study on the electrical and dielectric behaviour of Zn-substituted cobalt ferrialuminates. J. Phys. Condens. Matter **18**(34), 8063 (2006)
53. Z. Yan, J. Luo, Effects of CeZn co-substitution on structure, magnetic and microwave absorption properties of nickel ferrite nanoparticles. J. Alloys Compd. **695**, 1185–1195 (2017)
54. V. Lakhani et al., Structural parameters and X-ray Debye temperature determination study on copper-ferrite-aluminates. Solid State Sci. **13**(3), 539–547 (2011)
55. G. Kumar et al., Superparamagnetic behaviour and evidence of weakening in super-exchange interactions with the substitution of Gd3+ ions in the Mg–Mn nanoferrite matrix. Mater. Res. Bull. **63**, 216–225 (2015)
56. M.Z. Khan et al., Comprehensive study on structural, electrical, magnetic and photocatalytic degradation properties of Al3+ ions substituted nickel ferrites nanoparticles. J. Alloy. Compd. **848**, 155795 (2020)
57. S.B. Somvanshi et al., Structural, thermal, spectral, optical and surface analysis of rare earth metal ion (Gd3+) doped mixed Zn–Mg nano-spinel ferrites. Ceram. Int. **46**(9), 13170–13179 (2020)
58. S. Hassan et al., Structural, magnetic and electrochemical properties of Al-substituted Ni ferrites for energy storage devices. J. Energy Storage **55**, 105320 (2022)
59. S. Huo et al., Negative differential resistance with ultralow peak-to-valley voltage difference in Td-WTe2/2H-MoS2 heterostructure. Nano Lett. **24**(38), 11937–11943 (2024)
60. M. Ahmad et al., Influence of La-substitution and SiO2 additives on structure, magnetic and high frequency

dielectric properties of Co2W hexagonal ferrites synthesized by sol-gel auto-combustion method. J. Inorg. Organomet. Polym. Mater. (2025). https://doi.org/10.1007/s10904-024-03527-0

61. B. Rasool et al., Insight into the structural, magnetic and fluoride (F− 1) adsorption properties of copper–manganese ferrite (Cu0· 5Mn0· 5Fe2O4) and Azadirachta indica composites synthesized through hydrothermal method. Mater. Chem. Phys. **334**, 130415 (2025)
62. E. Petrova et al., Influence of synthesis methods on structural and magnetic characteristics of Mg–Zn-ferrite nanopowders. J. Magn. Magn. Mater. **473**, 85–91 (2019)
63. A. Anwar et al., Impact of rare earth Dy+ 3 cations on the various parameters of nanocrystalline nickel spinel ferrite. J. Mater. Res. Technol. **9**(3), 5313–5325 (2020)
64. M. Ahmad et al., Structural, morphological, mechanical, and electronic properties of nickel substituted manganese oxide (NixMn1-xO, x= 0.0, 0.2, 0.4) for electronic applications. Heliyon (2024). https://doi.org/10.1016/j.heliyon.2024.e26708
65. S. Mazen, H. Elsayed, N. Abu-Elsaad, A comparative study of different concentrations of (Co/Ni/Cu) effects on elastic properties of Li–Mn ferrite employing IR spectroscopy and ultrasonic measurement. Ceram. Int. **47**(19), 26635–26642 (2021)
66. M.N. Akhtar, M.A. Khan, Effect of rare earth doping on the structural and magnetic features of nanocrystalline spinel ferrites prepared via sol gel route. J. Magn. Magn. Mater. **460**, 268–277 (2018)
67. M.A. Almessiere et al., Structural, optical and magnetic properties of Tm3+ substituted cobalt spinel ferrites synthesized via sonochemical approach. Ultrason. Sonochem. **54**, 1–10 (2019)
68. S. Al-Sulaimi et al., Facile synthesis, structural, magnetic and enhanced fluoride (F−1) adsorptive properties of magnesium ferrite and oryza sativa composites. Mater. Chem. Phys. **339**, 130686 (2025)
69. T. Vigneswari, P. Raji, Structural, magnetic and optical properties of Al-substituted nickel ferrite nanoparticles. Int. J. Mater. Res. **109**(5), 413–421 (2018)
70. F. Saffari et al., Effects of co-substitution on the structural and magnetic properties of NiCoxFe_2−xO_4 ferrite nanoparticles. Ceram. Int. **41**(6), 7352–7358 (2015)
71. P. Van der Zaag, P. Van der Valk, M.T. Rekveldt, A domain size effect in the magnetic hysteresis of NiZn-ferrites. Appl. Phys. Lett. **69**(19), 2927–2929 (1996)
72. A. Hajalilou, S.A. Mazlan, A review on preparation techniques for synthesis of nanocrystalline soft magnetic ferrites and investigation on the effects of microstructure features on magnetic properties. Appl. Phys. A **122**, 1–15 (2016)
73. M.N. Akhtar et al., Systematic study of Ce3+ on the structural and magnetic properties of Cu nanosized ferrites for potential applications. J. Rare Earths **36**(2), 156–164 (2018)
74. Kao, K.C., 2004 *Dielectric phenomena in solids*. Elsevier.
75. C. Koops, On the dispersion of resistivity and dielectric constant of some semiconductors at audiofrequencies. Phys. Rev. **83**(1), 121 (1951)
76. Birajdar, A., et al., 2012 *Frequency and temperature dependent electrical properties of Ni0. 7Zn0. 3CrxFe*$_2$*−xO*$_4$ *(0≤ x≤ 0.5).* Ceram. Int. **38**(4): 2963–2970.
77. M.J. Iqbal, R.A. Khan, Enhancement of electrical and dielectric properties of Cr doped BaZn2 W-type hexaferrite for potential applications in high frequency devices. J. Alloys Compd. **478**(1–2), 847–852 (2009)
78. N. Rezlescu, E. Rezlescu, Dielectric properties of copper containing ferrites. Physica Status Solidi **23**(2), 575–582 (1974)
79. I. Ali et al., Electric and dielectric properties of Cr-Ga substituted BaM hexaferrites for high-frequency applications. J. Mater. Eng. Perform. **22**, 2673–2680 (2013)
80. M. El-Saadawy, DC conductivity for hexaferrites of the Zn2−xCuxBa1Fe16O27 system. J. Magn. Magn. Mater. **219**(1), 69–72 (2000)
81. A.M. Wahba, M.B. Mohamed, Structural, magnetic, and dielectric properties of nanocrystalline Cr-substituted Co0. 8Ni0. 2Fe_2O_4 ferrite. Ceram. Int. **40**(4), 6127–6135 (2014)
82. J. Park, J.-H. Lim, J.-H. Kang, J. Lim, H.W. Jang, H. Shin, S.H. Park, A review of understanding electrocatalytic reactions in energy conversion and energy storage systems via scanning electrochemical microscopy. J. Energy Chem. **91**, 155–177 (2024)
83. F. Wei, H. Wang, W. Ran, T. Liu, X. Liu, Preparation of S-N co-doped $CoFe_2O_4$ @ rGO@TiO_2 nanoparticles and their superior UV-Vis light photocatalytic activities. RSC Adv. **9**, 6152–6162 (2019)
84. L.L. Ding, L.Q. Wu, X.S. Ge, Y.N. Du, J.J. Qian, G.D. Tang, W. Zhong, Study of average valence and valence electron distribution of several oxides using X-ray photoelectron spectra. Res. Phys. **9**, 866–870 (2018)
85. Zeng, T., Meng, L., Li, Q., Liu, D., Zhou, Q., He, J.,... Yuan, C. (2025). Enhancing energetic disorder in all-organic composite dielectrics for high-temperature capacitive energy storage. Nature Communications, 16(1), 5620.
86. Wang, Q., Luo, R., Wang, Y., Fang, W., Jiang, L., Liu, Y.,... Niu, G. (2023). Set/Reset Bilaterally Controllable Resistance Switching Ga-doped Ge2Sb2Te5 Long-Term

Electronic Synapses for Neuromorphic Computing. Advanced Functional Materials, 33(19), 2213296.

87. Guan, Y., Yang, L., Chen, C., Wan, R., Guo, C.,... Wang, P. (2025). Regulable crack patterns for the fabrication of high-performance transparent EMI shielding windows. iScience, 28(1), 111543.
88. Sun, L., Jiang, Z., Yuan, B., Zhi, S., Zhang, Y., Li, J.,... Wu, A. (2021). Ultralight and superhydrophobic perfluorooctyltrimethoxysilane modified biomass carbonaceous aerogel for oil-spill remediation. Chemical Engineering Research and Design, 174, 71-78.
89. Xu, H., Wang, Y., Liu, M., & Zhai, Y. (2025). Alternating Multilayered Ti3C2Tx/Co Sandwich with Co Frosting for Superior Electromagnetic Wave Absorption Performance and Infrared Stealth Ability. ACS Applied Materials & Interfaces, 17(33), 47679-47695
90. Zhao, Z., Xu, X., Liu, W., & Wang, L. (2025). Modeling and suppression of magnetic noise in nanocrystalline magnetic shielding system considering residual loss magnetic noise and interlayer effects. Measurement, 250, 117216
91. Wang, C., Liu, J., Han, J., Zhang, Z., & Jiang, M. (2024). Analysis of Bidirectional Magnetic Field Modulation on Concentrated Winding Spoke-Type PM Machines. IEEE Transactions on Transportation Electrification, 10(3), 6076-6086
92. Cao, Y., Chi, H., Zhu, Z., Fan, S., Zhang, Y., Tang, Y.,... Hou, D. (2025). Multi-Functional Self-Sensing Electronic Gasket for Structural Health Monitoring of Transportation Pipelines. Advanced Functional Materials, 35(20), 2412634.

Publisher's Note Springer Nature remains neutral with regard to jurisdictional claims in published maps and institutional affiliations.

Springer Nature or its licensor (e.g. a society or other partner) holds exclusive rights to this article under a publishing agreement with the author(s) or other rightsholder(s); author self-archiving of the accepted manuscript version of this article is solely governed by the terms of such publishing agreement and applicable law.